Highlighting research by the group of Prof. Hao Jing at George Mason University, Fairfax VA, USA

Multi-shelled upconversion nanostructures with enhanced photoluminescence intensity *via* successive epitaxial layer-by-layer formation (SELF) strategy for high-level anticounterfeiting

Multi-shelled upconversion nanoparticles with significantly enhanced emission intensity are synthesized *via* successive epitaxial layer-by-layer formation (SELF) strategy and used in dual-modal anticounterfeiting and latent fingerprint detection.

As featured in:
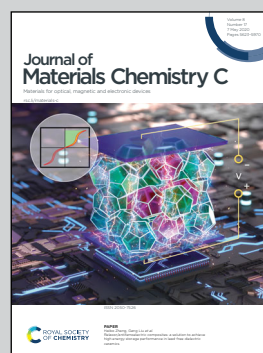
See Hao Jing *et al.*,
J. Mater. Chem. C, 2020, **8**, 5692.

ROYAL SOCIETY
OF CHEMISTRY

rsc.li/materials-c

PAPER

Multi-shelled upconversion nanostructures with enhanced photoluminescence intensity *via* successive epitaxial layer-by-layer formation (SELF) strategy for high-level anticounterfeiting†

Andrew J. Evangelista,[a] Mariia Ivanchenko,[a] Alline F. Myers,[b] Lisa N. McAnulty,[a] Gillian K. M. Payne[a] and Hao Jing ✩[a]

Owing to the ability to convert near-infrared (NIR) incident light into high-energy ultraviolet or visible light photons, lanthanide-doped upconversion nanoparticles (UCNPs) have attracted great attention in anticounterfeiting applications as appealing and unparalleled agents. To facilitate the efficient energy transfer and overcome the bottleneck of low upconverted photoluminescence, we report a one-pot successive epitaxial layer-by-layer formation (SELF) strategy based on ion layer adsorption and Ostwald ripening to synthesize a series of high-quality monodispersed multi-shelled UCNPs with narrow size distribution (coefficient of variation less than 5%). Up to 30 layers of uniform shell are successfully deposited by successive introduction of the shell precursor solutions, which results in fold change of 300 and 200 in upconverted emission intensities for Er^{3+} and Tm^{3+}-doped multi-shelled UCNPs, respectively. Using as-prepared multi-shelled UCNPs *via* SELF approach in conjunction with fabricated downconversion nanoparticles (DCNPs), we develop a facile and cost-effective strategy based on dual-modal manipulation of luminescence in anticounterfeiting to provide extra high-level security protection. The genuine pattern with true information is easier to visualize with the naked eye under excitation of 980 nm near-infrared (NIR) laser, while the false information could be readily read out when exposed to ultraviolet (UV) light. Meanwhile, latent fingerprint recognition with low background interference and distinguishable details in ridge patterns is achieved taking advantage of the significantly improved brightness in multi-shelled UCNPs.

1. Introduction

Societal instabilities and detrimental effects caused by illegal counterfeiting activities in currency, confidential documents, and pharmaceutical products around the world have become a global epidemic, which poses major security threats to individuals and the nation as a whole.[1–3] It is in great demand and therefore imperative to develop high-fidelity multilevel anticounterfeiting methods to combat these forgeries. During the past decades, considerable effects have been devoted to designing effective anticounterfeiting agents comprised of traditional luminescence materials such as fluorescent organic dyes,[4,5] inorganic semiconductor quantum dots[6–8] and perovskite nanocrystals[9,10] since they provided improved security due to the unique physical, chemical, and optical properties. However, the intrinsic drawbacks

such as photobleaching, spectral overlapping, and stringent need for multiple light sources to excite different species pose a considerable constraint for practical use of organic fluorophores and perovskite nanocrystals. The toxicity of heavy metals and unavoidable background fluorescence from substrates under excitation of ultraviolet (UV) light obstruct the applications of quantum dots.[11] In striking contrast, rare-earth or lanthanide-doped upconversion nanoparticles (UCNPs) with well-controlled structures and morphologies as another attractive alternative luminescent material circumvents the aforementioned weaknesses.[12] The unique and remarkable optical characteristics of UCNPs, such as large anti-Stokes shifts, sharp and tunable multi-peak line emission profiles, constant light emitting capabilities and excellent photostability,[13–19] owing to their ability to convert near-infrared (NIR) incident light into high-energy ultraviolet or visible light photons, make them appealing and unparalleled in anticounterfeiting applications since first observed and formulated in the 1960s.[20–22] The elimination of background auto-fluorescence/interference from either endogenous fluorophores or non-specifically bound probes, by using a low-energy near-infrared (NIR) laser as the excitation source, enables UCNPs to be

[a] *Department of Chemistry and Biochemistry, George Mason University, Fairfax, Virginia 22030, USA. E-mail: hjing2@gmu.edu; Fax: +1-703-993-1040; Tel: +1-703-993-5221*

[b] *National Institute of Standards and Technology (NIST), 100 Bureau Dr, Gaithersburg, Maryland 20899, USA*

† Electronic supplementary information (ESI) available. See DOI: 10.1039/d0tc00902d

superior anticounterfeiting agents with enhanced signal-to-noise ratio, otherwise unattainable through their counterparts such as quantum dots (QDs) and organic dyes.

Although a plethora of modalities such as excitation power,[23] pulse duration,[24] phase angle[11] temperature,[25,26] lifetime,[27–29] and morphological control[30–34] were demonstrated in the past few years to modulate the emission color profiles of UCNPs in proof-of-concept anticounterfeiting, the bottleneck of low upconversion efficiency (usually less than 1%) inherent to UCNPs continues to hinder and limit their practical utility in high-end encryption applications.[35–38] It was experimentally demonstrated that the epitaxial growth of a shell with negligent lattice mismatch onto hexagonal β-UCNP cores *via* seed-mediated heat-up approach was an effective route to facilitate efficient energy transfer and improve the optical properties.[39–45] However, the fact that nonuniform shell formation[46–48] and bimodal size distribution[49] of the obtained core–shell hybrid nanostructures were always observed during the reaction makes it difficult to reproduce the consistent outcomes or maintain the stability of UCNPs. In addition, this widely used seed-mediated protocol is not flexible, especially for the synthesis of multi-shelled UCNPs, in that lengthy volatile solvent-removing and cooling cycles must be repeated multiple times during the growth of every layer of shell and are considered to be laborious and time-consuming. Despite the mention of multi-shelled UCNPs in a few reports,[43,50] it is still challenging to correlate the shell thickness and enhancement in overall UC emission intensity since only the growth of a limited number of layers of shell was achieved.

In this study, a one-pot successive epitaxial layer-by-layer formation (SELF) strategy based upon ion layer adsorption and Ostwald ripening is introduced to fabricate a series of high-quality multi-shelled UCNPs with the coefficient of variation (CV) less than 5%. Up to 30 layers of shell are successfully deposited by successive introduction of the shell precursor solutions at a high temperature. Contrary to the generally assumed mechanism in which core UCNPs act as seeds or nuclei for subsequent shell growth, the shell precursors preferentially nucleate in SELF synthesis, followed by a ripening-mediated process leading to the formation of core–shell UCNPs. Remarkably, the overall enhancement in upconverted luminescence emission intensities of 30-shell layered β-NaYF$_4$:Yb^{3+}/Er^{3+}@NaYF$_4$ and 30-shell layered β-NaYF$_4$:Yb^{3+}/Tm^{3+}@NaYF$_4$ hybrid UCNPs are able to reach as high as 300-fold and 200-fold, respectively, due to the efficient surface defects passivation effect. Physically intermingled with Eu^{3+}-doped downconversion nanocrystals (DCNPs designated as NaGdF$_4$:Ce^{3+}@NaGdF$_4$:Eu^{3+}) which absorb high-energy radiation and emit low-energy photons,[51] a facile and cost-effective strategy based on dual-modal manipulation of luminescence is realized and utilized in anticounterfeiting to elevate the difficulty of illegal imitation and provide extra high-level security protection. Previous research, such as creating anti-counterfeiting patterns using luminescent nanotaggants excited at distinct wavelengths,[52] indicates that high throughput multiplexed encoding is a powerful tool for anticounterfeiting. Besides the up-conversion luminescence, studies on the down-conversion luminescence properties further enrich the parameters used for optical encoding, including

excitation wavelength, emission wavelength and lifetime.[53–57] In striking contrast to the previous approaches, in which both upconversion and downconversion ions are either uniformly doped into the same matrix[58,59] or different layers within the same nanostructure,[60–62] our dual-mode system is not susceptible to the detrimental cross-relaxation. More importantly, benefiting from the significantly enhanced brightness in multi-shelled UCNPs synthesized by the SELF method, the genuine pattern with true information is guaranteed and much easier to distinguish with the naked eye under excitation of near-infrared (NIR) irradiation and substantially expands the encryption capacity. We have demonstrated that the fake information could be read out under UV light excitation, while the true information was readily given out under 980 nm NIR laser irradiation when upconversion and downconversion nanophosphors were collaboratively applied in the same region but with different labelling patterns. Furthermore, the as-prepared multi-shell UCNPs with significantly enhanced luminescence intensity have been employed in latent fingerprint (LFP) imaging, providing distinguishable details of ridge patterns and, therefore, facilitating the application of SELF synthesis in the realm of personal identification, forensic science, and security.

2. Experimental details

2.1 Materials

Yttrium(III) acetate hydrate (Y(CH$_3$CO$_2$)$_3$·xH$_2$O, 99.9%), gadolinium(III) acetate hydrate (Gd(CH$_3$CO$_2$)$_3$·xH$_2$O, 99.9%), ytterbium(III) acetate tetrahydrate (Yb(CH$_3$CO$_2$)$_3$·4H$_2$O, 99.9%), erbium(III) acetate hydrate (Er(CH$_3$CO$_2$)$_3$·xH$_2$O, 99.9%), thulium(III) acetate hydrate (Tm(CH$_3$CO$_2$)$_3$·xH$_2$O, 99.9%), europium(III) acetate hydrate (Eu(CH$_3$CO$_2$)$_3$·xH$_2$O, 99.9%), oleic acid (OA, 90%), 1-octadecene (ODE, 90%), ammonium fluoride (NH$_4$F, 99.99%), sodium hydroxide (NaOH, 98%), cyclohexane (C$_6$H$_{12}$, anhydrous, 99.5%), methanol (CH$_3$OH, 99.9%), dichloromethane (CH$_2$Cl$_2$, 99.8%), sodium citrate tribasic dihydrate (HOC(COONa)(CH$_2$COONa)$_2$·2H$_2$O, 99%) and nitrosyl tetrafluoroborate (NOBF$_4$, 95%) were all purchased from Sigma-Aldrich. Ethanol (95%) was purchased from VWR. All the chemicals were used as received without further purification. The deionized water used in the experiment was ultra-pure (MilliQ, 18 MΩ).

2.2 Characterization

The size and morphology of nanoparticles (both upconversion and downconversion) were determined by using an FEI Titan 80–300 analytical transmission electron microscope (TEM) operating at 300 kV. The standard TEM samples were prepared by dropping solutions of nanoparticles dispersed in cyclohexane onto the surface of copper grids. Fourier transform infrared (FTIR) spectra were obtained from samples in KBr pellets using an Agilent Technologies Cary 630 spectrometer. Upconversion luminescence (UCL) spectra were recorded at room temperature on a high-sensitivity spectrofluorometer (QE Pro-FL, Ocean Optics) with the excitation source of an external 0–5 W adjustable continuous wave 980 nm laser diode (Dragon Lasers, China). Down-conversion luminescence spectra were obtained at room temperature *via* a

This journal is © The Royal Society of Chemistry 2020

J. Mater. Chem. C, 2020, **8**, 5692–5703 | **5693**

RF-6000 fluorospectrometer (Shimadzu) with a xenon lamp as the excitation source. All digital photographs were taken using Nikon D7000 16.2 Megapixel digital single-lens reflex camera (DSLR) with 18–140 mm lens and high-resolution CMOS sensor.

2.3 Synthesis of β-NaYF$_4$:Yb^{3+}/Er^{3+} (18/2 mmol%) core UCNPs

In a typical procedure, 0.5 mmol of Ln(CH$_3$CO$_2$)$_3$ (Ln = Y, Yb and Er) including 0.11 g of Y(CH$_3$CO$_2$)$_3$, 38 mg of Yb(CH$_3$CO$_2$)$_3$, and 100 μL of 0.1 mol L^{-1} aqueous Er(CH$_3$CO$_2$)$_3$ were mixed with OA/ODE (volume ratio of 3/7.5) in a three-neck round bottom flask (50 mL) and degassed at 150 °C for 30 min with stirring to remove water before cooling down to 50 °C. Then, 10 mL of a methanol solution containing NaOH (0.05 g) and NH$_4$F (0.074 g) was added into the mixture and stirred under argon protection at 50 °C for 30 min before removing methanol at 70 °C under vacuum. The temperature was then increased to 150 °C under vacuum to remove low boiling point solvents and residual moisture. After 30 min, the mixture was heated to 290 °C and kept for 1.5 h under the protection of Ar. After the solution cooled down to room temperature, the prepared core UCNPs were collected by addition of ethanol, washed with cyclohexane and ethanol several times, and re-dispersed in 4 mL of cyclohexane (10 mg mL^{-1}) and stored at 4 °C for future use.

2.4 Synthesis of β-NaYF$_4$:Yb^{3+}/Tm^{3+} (27/0.3 mmol%) Core UCNPs

This protocol is identical to the one for β-NaYF$_4$:Yb^{3+}/Er^{3+} except for the amounts of Yb(CH$_3$CO$_2$)$_3$ and Tm(CH$_3$CO$_2$)$_3$. 36.1 mg Yb(CH$_3$CO$_2$)$_3$ and 10 μL of 0.1 mol L^{-1} aqueous Tm(CH$_3$CO$_2$)$_3$ were used instead in the synthesis of β-phase NaYF$_4$:Yb^{3+}/Tm^{3+} nanoparticles.

2.5 Preparation of yttrium–oleate precursors

For the yttrium–oleate host precursor solution with the concentration of 0.1 mol L^{-1} (denoted as Y–OA), 0.47 g Y(CH$_3$CO$_2$)$_3$ was mixed with OA/ODE (volume ratio of 5/12.5) in a three-neck round bottom flask and heated at 140 °C for at least 30 min under vacuum with magnetic stirring to remove residual oxygen and water. A clear homogeneous solution formed before cooling down to 90 °C for future use.

2.6 Preparation of fluoride–oleate precursors

The fluoride–oleate precursor (denoted as F–OA) with concentration of 0.4 mol L^{-1} was prepared by adding NaOH (0.21 g) and NH$_4$F (0.31 g) pre-dissolved in methanol (21 mL) to OA/ODE (volume ratio of 6/15). The mixtures were heated first under vacuum with magnetic stirring to 70 °C for at least 2 hours to remove methanol and then to 140 °C to remove residual water and low boiling point solvent before cooling down to 90 °C for future use.

2.7 Preparation of β-NaYF$_4$:Yb^{3+}/Er^{3+}@NaYF$_4$ UCNPs with multiple shell thickness *via* SELF strategy

Briefly, 4 mL of the purified β-NaYF$_4$:Yb^{3+}/Er^{3+} (18/2 mmol%) core UCNPs in cyclohexane were mixed with 3 mL of OA and 7.5 mL of ODE in a 100 mL three-neck round bottom flask with magnetic stirring. Then, the mixture was heated to 70 °C under vacuum for 30 min to remove cyclohexane and any residual air

and then to 150 °C for another 30 min to remove other low boiling point solvents. Subsequently, the temperature was increased to 290 °C under the protection of Ar. Then, 0.5 mL of Y–OA and 0.5 mL of F–OA precursor solutions were simultaneously injected into the reaction and kept for 15 min to allow NaYF$_4$ shell growth. Each fast injection indicated one layer of NaYF$_4$, and the injection cycles were repeated 30 times to obtain core–shell UCNPs with 30 layers. Various aliquots (0.4 mL, 0.8 mL, 1.2 mL and 1.6 mL corresponding to 0 layer, 10 layers, 20 layers, and 30 layers, respectively) were taken out from the parental mixture after every 10 injections, centrifuged, and washed by cyclohexane and ethanol before being re-dispersed in 1 mL pure cyclohexane for analysis. In 7.5 hours when the reaction was complete, the mixture was cooled down to room temperature and purified by the same procedure as the core UCNPs.

2.8 Preparation of β-NaYF$_4$:Yb^{3+}/Tm^{3+}@NaYF$_4$ UCNPs with multiple shell thickness *via* SELF strategy

Identical procedures were adopted except that 4 mL purified β-NaYF$_4$:Yb^{3+}/Tm^{3+} (27/0.3 mmol%) core UCNPs in cyclohexane were utilized.

2.9 Synthesis of NaGdF$_4$:Ce^{3+}(15%)@NaGdF$_4$:Eu^{3+} (5%) down-conversion NPs

In a typical procedure, 0.114 g (0.34 mmol) Gd(CH$_3$CO$_2$)$_3$ and 19 mg (0.06 mmol) Ce(CH$_3$CO$_2$)$_3$ were mixed with OA (4 mL) and ODE (6 mL) in a 50 mL three-neck round bottom flask. The mixture was heated to 150 °C under vacuum with magnetic stirring to remove oxygen and water. After cooling down to 50 °C, a methanol solution containing NaOH (1 mmol) and NH$_4$F (1.28 mmol) was added and stirred for 30 min under Ar protection. Subsequently, the temperature was increased to 70 °C to remove methanol and then to 150 °C to remove low boiling point solvents and volatile impurities under vacuum. Then the mixture was heated to 290 °C and kept at this temperature for 1.5 h under the protection of argon before cooling down to room temperature and being collected by addition of ethanol. The obtained NaGdF$_4$:Ce^{3+}(15%) core nanoparticles were washed with cyclohexane and ethanol several times, and re-dispersed in 4 mL cyclohexane. The synthesis of NaGdF$_4$:Eu^{3+} (5%) shell was the same as to that of the core nanoparticles except that 0.127 g (0.38 mmol) Gd(CH$_3$CO$_2$)$_3$ and 6.6 mg (0.02 mmol) Eu(CH$_3$CO$_2$)$_3$ were used in the protocol.

2.10 Anti-counterfeiting application

Colloidal solutions of upconversion and down-conversion nanoparticles in cyclohexane were used as ink to be injected into the character marks in the polymethylmethacrylate (PMMA) plate. For the PMMA plate with character marks of GMU, the solution of down-conversion nanoparticles (NaGdF$_4$:Ce^{3+}@NaGdF$_4$:Eu^{3+}) was first injected to only cover a partial portion of three letters to manifest CVJ under excitation of UV lamp as the fake information. The solution of upconversion nanoparticles (β-NaYF$_4$:Yb^{3+}/Er^{3+}@ NaYF$_4$ or β-NaYF$_4$:Yb^{3+}/Tm^{3+}@NaYF$_4$) was then injected to label the three whole characters as true information such that the labeled characters of "GMU" were read out under excitation of 980 nm NIR laser. To enhance the applicability of this anti-counterfeiting

5694 | *J. Mater. Chem. C*, 2020, **8**, 5692–5703

This journal is © The Royal Society of Chemistry 2020

method, the solution of down-conversion nanoparticles (NaGdF₄:Ce³⁺@NaGdF₄:Eu³⁺) was also employed to another PMMA plate with character marks of 888 for labelling as the fake information. Within the same characters (888), the solution of upconversion nanoparticles (β-NaYF₄:Yb³⁺/Er³⁺@NaYF₄ or β-NaYF₄:Yb³⁺/Tm³⁺@NaYF₄) was injected to label pattern "7", "0" and "3", respectively as the true information. Under UV lamp excitation, "888" was read out as the fake information while the true information of the area code "703" was exhibited and identified with the excitation of 980 nm NIR laser.

2.11 Preparation of citrate-functionalized multi-shelled UCNP for latent fingerprint imaging

Firstly, ligand-free UCNPs in aqueous solution were obtained through a ligand exchange strategy. In a typical procedure, as-synthesized oleic acid (OA)-capped multi-shelled UCNPs in cyclohexane (either β-NaYF₄:Yb³⁺/Er³⁺@NaYF₄ or β-NaYF₄:Yb³⁺/Tm³⁺@NaYF₄) were mixed with a dichloromethane solution of NOBF₄ (0.02 mol L⁻¹) at room temperature. In 5 min, the precipitation of nanoparticles was observed. After centrifugation to remove the supernatant, ethanol was added to wash the nanoparticles several times to obtain ligand-free multi-shelled UCNPs. These UCNPs were re-dispersed in aqueous trisodium citrate solution (10 mg mL⁻¹) and allowed to incubate overnight. Citrate-functionalized multi-shelled UCNPs were obtained after centrifugation and rinsed with deionized water.

2.12 Preparation of multi-shelled UCNP powder for latent fingerprint imaging

In a typical procedure, the as-synthesized oleic acid capped multi-shelled UCNPs in cyclohexane (β-NaYF₄:Yb³⁺/Tm³⁺@NaYF₄) were washed several times with ethanol and dispersed in cyclohexane. The UCNP solution was then dried in an oven at 75 °C overnight. The dry UCNPs were ground into a fine dust *via* mortar and pestle and stored.

2.13 Latent fingerprint collection and incubation

For the deposition of latent fingerprint, volunteers were asked to wash their hands with soap and water and then to touch their foreheads and their hands together before pressing their fingers on the surface of glass slides. For the solution incubation, first the fingerprint-deposited glass slides were rinsed with deionized water for about 2 min, then immersed into aqueous solution of trisodium citrate functionalized UCNPs for 30 min, and then finally rinsed with deionized water for another 2 min, gently. The glass slides were dried in air before imaging. For the powder deposition, the powder was deposited onto the fingerprint and allowed to adhere for at least 30 min. The excess was then gently blown away with air before imaging.

3. Results and discussion

3.1 Upconversion photoluminescence properties of core–shell UCNPs with different shell layers *via* SELF approach

Lanthanide ions are considered promising luminescent centers due to their abundant energy levels. However, the 4f–4f intra-configurational forbidden transition has a low probability of occurring.[63] The emission can be restored by embedding free lanthanide ions in an inorganic matrix to partially break the parity-forbidden rule so that an allowed transition has a high probability of occurring.[64] NaYF₄ is chosen as the host matrix due to its low lattice phonon energies and high upconversion efficiency. The energy-level diagram and energy transfer pathways in Er³⁺-doped UCNPs (β-NaYF₄:Yb³⁺/Er³⁺) are shown in Fig. 1A and have been extensively investigated previously.[64] After the pump photon is absorbed by ytterbium (Yb³⁺) ions leading to $^2F_{7/2} \rightarrow {^2F_{5/2}}$ transition and the energy is resonantly transferred to adjacent erbium (Er³⁺) ions in the matrix under the excitation of 980 nm near-infrared (NIR) laser, three distinct non-radiative relaxations occur, yielding $^2H_{11/2} \rightarrow {^4I_{15/2}}$ (528 nm), $^4S_{3/2} \rightarrow {^4I_{15/2}}$ (541 nm), and $^4F_{9/2} \rightarrow {^4I_{15/2}}$ (656 nm) emissions assigned to two-photon upconversion processes (Fig. 1A). The experimentally measured upconversion photoluminescence spectra of the core–shell UCNPs with different shell layers show a significant enhancement in emission intensity during the growth of the NaYF₄ shell, which results from the passivation of surface defects (Fig. 1B). The fold change (comparing with the core UCNPs) of core–shell UCNPs with 30 shell layers at 541 nm and 656 nm can reach more than 300 and 200, respectively (Fig. 1C). This is further demonstrated in the digital photographs of multi-shelled β-NaYF₄:Yb³⁺/Er³⁺@NaYF₄ UCNPs under 980 nm laser irradiation (power density: 15 W cm⁻²) in Fig. 1D.

To further demonstrate the rationale, the one-pot successive epitaxial layer-by-layer formation (SELF) strategy is extended to other UCNPs doped with Yb³⁺–Tm³⁺ as sensitizer and activator, respectively. In contrast to Yb³⁺–Er³⁺ co-doped UCNPs, four multi-phonon nonradiative relaxations, including $^1D_2 \rightarrow {^3F_4}$ (450 nm), $^1G_4 \rightarrow {^3H_6}$ (475 nm), $^1D_2 \rightarrow {^3H_5}$ (540 nm), and $^3H_4 \rightarrow {^3H_6}$ (802 nm) are generated in the energy-level diagram of core–shell β-NaYF₄:Yb³⁺/Tm³⁺ UCNPs under 980 nm NIR laser excitation due to the discretely arranged energy levels of Tm³⁺ ions (Fig. 2A). It is noteworthy to point out that the rare energy level transition of $^1D_2 \rightarrow {^3H_5}$ at 540 nm is excited and detectable in this multishelled nanostructure obtained by SELF, despite that it is weak due to the low transition probabilities.[65–67] The emission intensities of the three characteristic peaks in upconversion photoluminescence spectra increase significantly as the shell thickness increases (Fig. 2B). Based on the correlation between fold change and the number of shell layers, the peak emissions in 450 nm and 475 nm are about 200 and 100 times higher than the core UCNPs, respectively, as the shell layers reach 30 in the SELF synthesis (Fig. 2C). The brightness of the colloidal solutions of multi-shelled β-NaYF₄:Yb³⁺/Tm³⁺@NaYF₄ UCNPs increases from the originally negligible blue to a readily distinguished glare under 980 nm laser excitation (Fig. 2D).

3.2 Morphology and structure properties of core–shell UCNPs with different shell layers

To prepare shell-thickness-controllable β-NaYF₄:Yb³⁺/Er³⁺@NaYF₄ UCNPs *via* SELF approach, β-NaYF₄:Yb³⁺/Er³⁺ core UCNPs are first synthesized. Two solutions of shell precursors dissolved

This journal is © The Royal Society of Chemistry 2020

J. Mater. Chem. C, 2020, **8**, 5692–5703 | **5695**
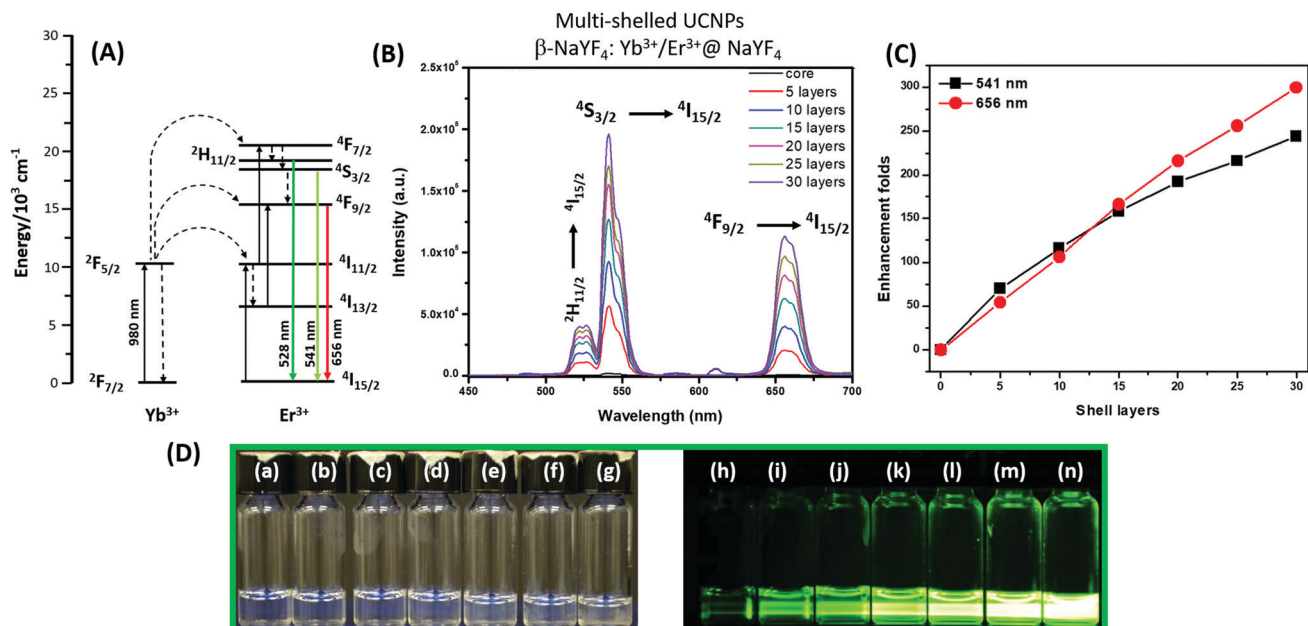
Fig. 1 (A) Energy-level diagram of β-NaYF$_4$:Yb^{3+}/Er^{3+} UCNPs under 980 nm NIR laser excitation. (B) Up-conversion photoluminescence spectra and (C) correlation between fold change in peaks with wavelengths at 541 nm and 656 nm and the number of shell layers, and (D) digital photographs of β-NaYF$_4$:Yb^{3+}/Er^{3+}@NaYF$_4$ UCNPs with multiple shell thickness obtained *via* SELF approach. (a)–(g) Ambient light photographs of 0, 5, 10, 15, 20, 25, 30 layers, respectively. (h)–(n) Emission from 980 nm NIR laser excitation of 0, 5, 10, 15, 20, 25, 30 layers, respectively (power density: 15 W cm^{-2}, UCNPs concentration: 1 mg mL^{-1}).
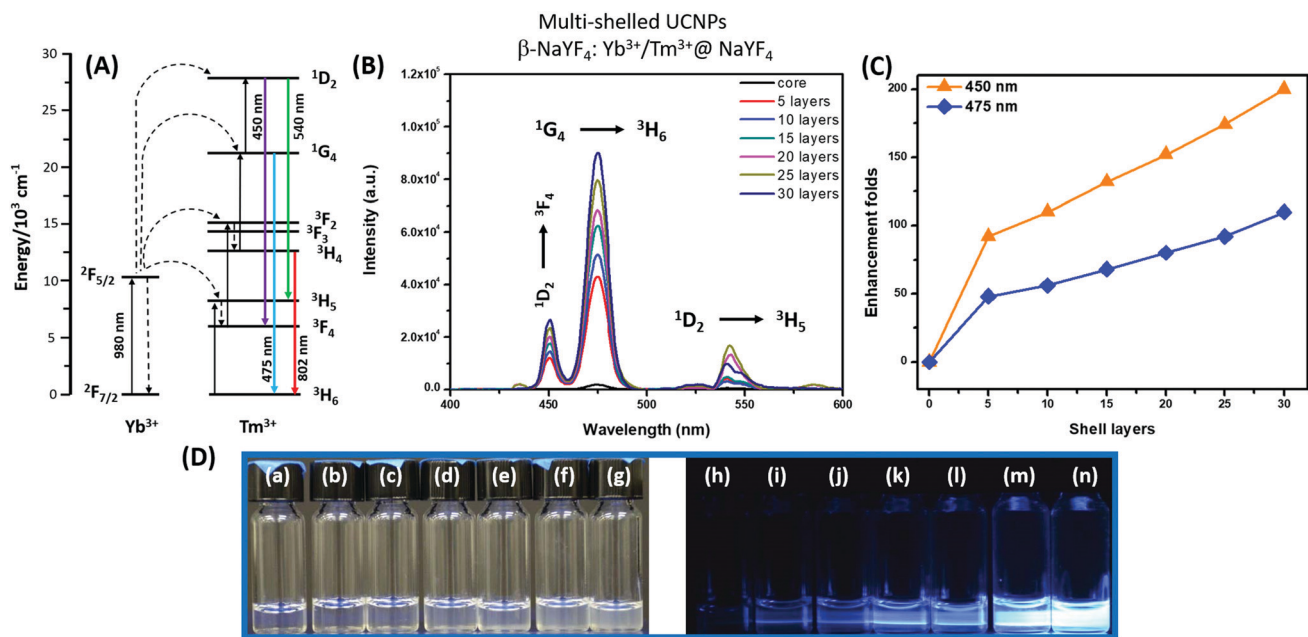
Fig. 2 (A) Energy-level diagram of β-NaYF$_4$:Yb^{3+}/Tm^{3+} UCNPs under 980 nm NIR laser excitation. (B) Up-conversion photoluminescence spectra and (C) correlation between fold change in peaks with wavelengths at 450 nm and 475 nm and the number of shell layers, and (D) digital photographs of β-NaYF$_4$:Yb^{3+}/Tm^{3+}@NaYF$_4$ UCNPs with multiple shell thickness obtained *via* SELF approach. (a)–(g) Ambient light photographs of 0, 5, 10, 15, 20, 25, 30 layers, respectively. (h)–(n) Emission from 980 nm NIR laser excitation of 0, 5, 10, 15, 20, 25, 30 layers, respectively (power density: 15 W cm^{-2}, UCNPs concentration: 1 mg mL^{-1}).

in the mixture of OA and ODE (volume ratio of 0.4), including yttrium–oleate and fluoride–oleate precursors, are degassed under vacuum at 140 °C before being simultaneously injected into the reaction and kept for 15 min at 290 °C under the protection of argon to allow NaYF$_4$ shell growth. In SELF method, the shell precursors are simultaneously and successively introduced/injected into the reaction solution after the uniform seed particles/nuclei are pre-formed. The "monomers"

due to the decomposition of shell precursors at a higher temperature are supplied to precipitate on the surface of the existing nuclei. The monomer concentration from each individual injection is kept very low during growth to suppress the unwanted homogeneous nucleation in that its production and consumption maintains balance. Hence, the monomers released could be continuously consumed to deposit on the core UCNPs without homogeneous nucleation. And because the seed particles/core UCNPs synthesized are quite uniform (confirmed in Fig. 3A and E), the monodisperse multi-shelled UCNPs can be successfully produced by using SELF approach. In addition, the ripening time (15 min) between each injection facilitates UCNPs with narrow size distribution, as the UCNPs spontaneously self-focus by dissolution of the energetically less favored monomers in the ensemble, referred to as Ostwald ripening dynamics. The 15 min ripening facilitates the epitaxial growth of shell on hexagonal phase core UCNPs to form core–shell UCNPs with narrow size distribution by dissolving the energetically less favored small particles. Each injection indicates one monolayer of $NaYF_4$, and the injection cycles were repeated 30 times successively to obtain core–shell β-$NaYF_4$:Yb^{3+}/Er^{3+}@$NaYF_4$ UCNPs with 30 layers. The synthesis of β-$NaYF_4$:Yb^{3+}/Tm^{3+}@$NaYF_4$ with different shell thickness is achieved similarly except that the cores of β-$NaYF_4$:Yb^{3+}/Tm^{3+} are used in the protocol. After every 10 injections, different aliquots are taken out from the mixture during SELF synthesis and washed for microscopy analysis. The morphology and structure of β-$NaYF_4$:Yb^{3+}/Er^{3+} and β-$NaYF_4$:Yb^{3+}/Tm^{3+} core UCNPs, as well as the corresponding core–shell UCNPs with 10, 20, and 30 layers, are further demonstrated by transmission electron microscopy (TEM) images, showing that the cores have

gradually grown into larger particles with retained hexagonal phase and the $NaYF_4$ shell adapts the crystal lattice of core UCNPs (Fig. 3). The average size for β-$NaYF_4$:Yb^{3+}/Er^{3+} and β-$NaYF_4$:Yb^{3+}/Tm^{3+} core UCNPs are 28.2 nm $\pm$ 1.2 nm, and 22.2 nm $\pm$ 0.7 nm (errors are standard deviations). After 30 additional layers the dimensions increase to 45.2 nm $\pm$ 1.3 nm and 34.2 nm $\pm$ 1.6 nm (errors are standard deviations), respectively. According to the statistical histograms, a narrow unimodal size distribution with the coefficient of variation (σ) less than 5% is obtained by analyzing more than 150 nanoparticles for all samples, even for the core–shell UCNPs with 30 layers, further confirming the uniformity (Fig. S1, ESI†).

High-resolution TEM (HR-TEM) images show a single crystalline grain of the β-$NaYF_4$:Yb^{3+}/Er^3 core UCNPs (Fig. 4A). The interplanar spacing of the lattice planes measured from HR-TEM image is 0.515 nm, which is in accordance with the lattice parameters of the (100) plane of β phase $NaYF_4$ (Fig. 4B). The fast Fourier transform (FFT) diffractogram shown in Fig. 4C indicates the hexagonal phase of nanoparticles synthesized, which is further confirmed by the magnified HR-TEM image showing the atomic arrangement in a hexagonal shape (Fig. 4D).

3.3 Photoluminescence properties of NaGdF$_4$:Ce^{3+}@NaGdF$_4$:Eu^{3+} downconversion nanoparticles

To achieve the dual-modal manipulation of luminescence and utilization in anticounterfeiting, downconversion nanoparticles are then synthesized via conventional thermal decomposition method besides UCNPs. For downcoversion nanoparticles, we adopt a core–shell structure with the sensitizer (Ce^{3+}) and activator (Eu^{3+}) incorporated into separated layers at precisely
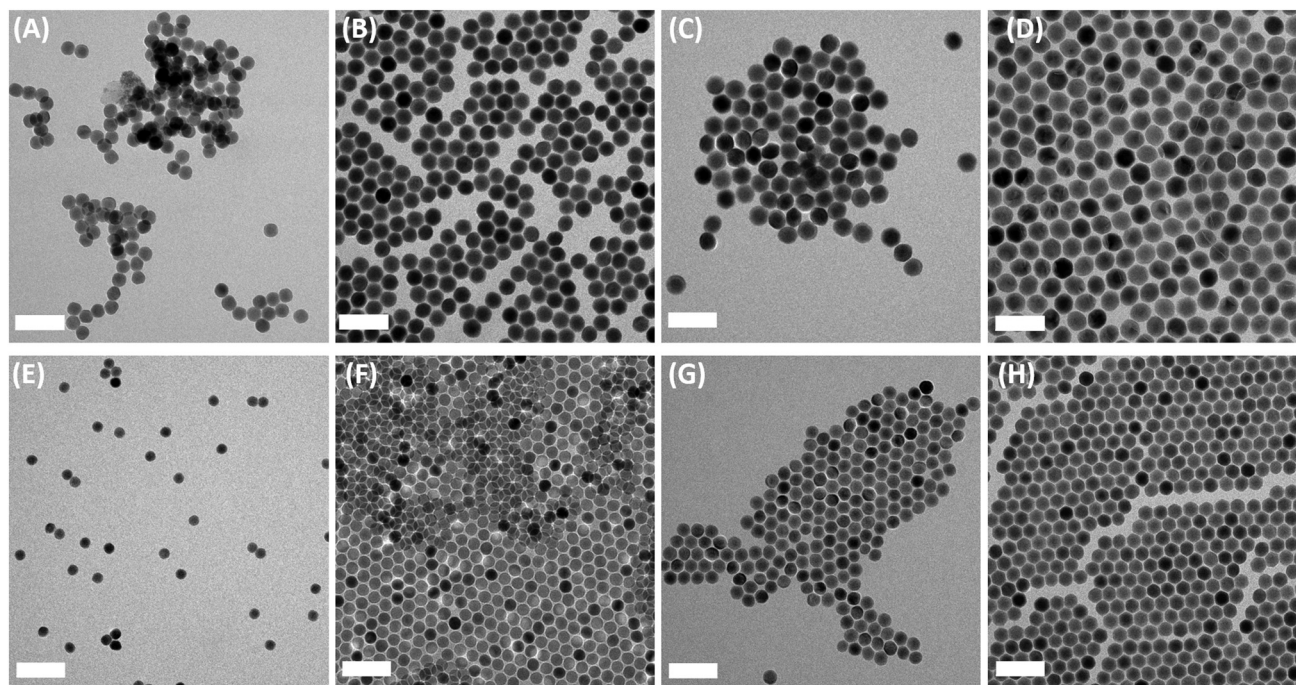
Fig. 3 TEM images of β-$NaYF_4$:Yb^{3+}/Er^{3+}@$NaYF_4$ UCNPs with (A) 0, (B) 10, (C) 20, (D) 30 shell layers and β-$NaYF_4$:Yb^{3+}/Tm^{3+}@$NaYF_4$ UCNPs with (E) 0, (F) 10, (G) 20, (H) 30 shell layers. Scale bar is 100 nm.

This journal is © The Royal Society of Chemistry 2020

J. Mater. Chem. C, 2020, 8, 5692–5703 | 5697
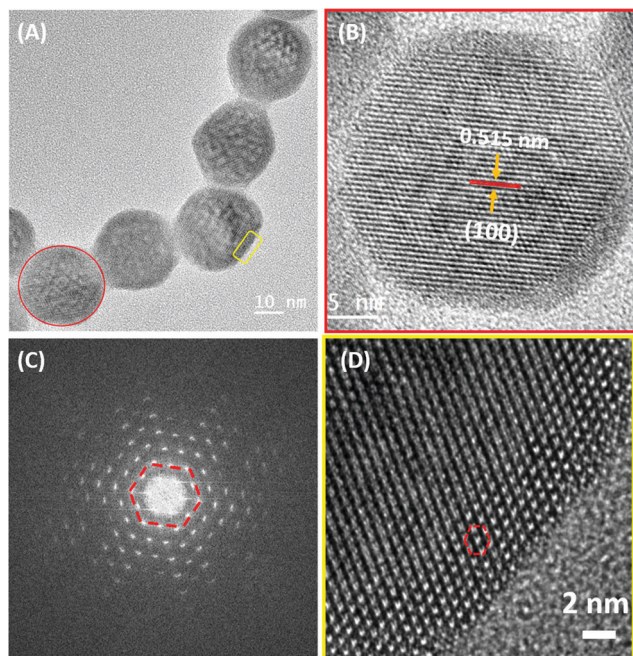
Fig. 4 (A) High-resolution (HR-TEM) image of monodisperse β-NaYF$_4$:Yb^{3+}/Er^3 core UCNPs and (B) enlarged image of one UCNP particle circled in red in panel A. (C) Fast Fourier Transform (FFT) pattern of the region encompassing the whole cross section of UCNPs in panel B. (D) Zoomed-in atomic resolution image of the UCNP particle highlighted in yellow in panel A.

defined concentrations to ensure the efficient energy migration through gadolinium (Gd) sublattice by eliminating the deleterious cross-relaxation.[49,68] According to the energy-level diagram, the excited state of Ce^{3+} is first populated under the ultraviolet excitation, and then an energy migration process in Gd sublattice bridges energy transfer from Ce^{3+} to Eu^{3+} ions (Fig. 5A). The characteristic emission peaks of NaGdF$_4$:Ce^{3+}@NaGdF$_4$:Eu^{3+} downconversion nanoparticles at 592 nm, 614 nm, and 696 nm observed in the experimentally measured photoluminescence

spectrum can be assigned to three transitions of Eu^{3+} ions under excitation of UV light: $^5D_0 \rightarrow {}^7F_1$, $^5D_0 \rightarrow {}^7F_2$, $^5D_0 \rightarrow {}^7F_4$, respectively (Fig. 5B). In addition, the digital photographs of colloidal NaGdF$_4$:Ce^{3+}@NaGdF$_4$:Eu^{3+} nanoparticles are displayed in Fig. 5C, showing the transparency of the solution without irradiation and the distinctive red/pink color under UV light excitation.

3.4 Dual-mode manipulation of multi-shelled UCNPs and downconversion nanoparticles in anticounterfeiting applications

In order to encrypt the anticounterfeiting information, we first inject the colloidal solutions of multi-shelled UCNPs and down-conversion nanoparticles into different regions of the character marks engraved on the surface of the polymethylmethacrylate (PMMA) plate as shown in the schematic illustration (Fig. 6A and B). The anticounterfeiting information can be extracted under excitation of two different light sources (254 nm and 980 nm). Taking the character marks of GMU on PMMA plate as an example, the solution of NaGdF$_4$:Ce^{3+}@NaGdF$_4$:Eu^{3+} down-conversion nanoparticles (DCNPs) is injected to only cover a partial portion of three letters to manifest CVJ as the fake information. Meanwhile, the solution of core–shell β-NaYF$_4$:Yb^{3+}/Er^{3+}@NaYF$_4$ UCNPs with 30 layers is applied to label three whole letters as true information. As a result, fake information ("CVJ") in the pink color is displayed under excitation of ultraviolet lamp (Fig. 6C), whereas true patterns ("GMU") in the green color can only be read out when exposed to 980 nm near-infrared laser (Fig. 6E). This is only made possible due to the significant enhancement in upconversion photoluminescence intensities from the successive epitaxial layer-by-layer formation (SELF) approach. As a control experiment, the β-NaYF$_4$:Yb^{3+}/Er^{3+} core UCNPs are also employed to label the patterns. However, they are not bright enough to provide any useful information in the image under irradiation of 980 nm laser, which is consistent with weak
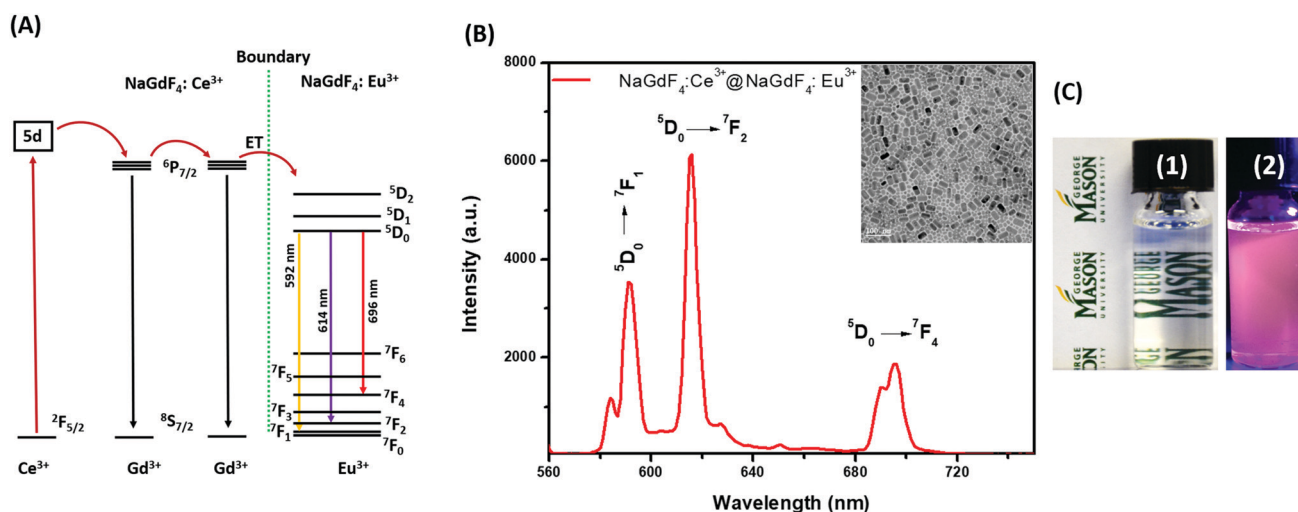
Fig. 5 (A) Energy-level diagram and (B) photoluminescence spectrum of NaGdF$_4$:Ce^{3+}@NaGdF$_4$:Eu^{3+} downconversion nanoparticles with the inset of TEM image. (C) Digital photographs of colloidal solutions of NaGdF$_4$:Ce^{3+}@NaGdF$_4$:Eu^{3+} downconversion nanoparticles in cyclohexane (1) without irradiation showing its transparency and (2) under excitation of ultraviolet (UV) light.
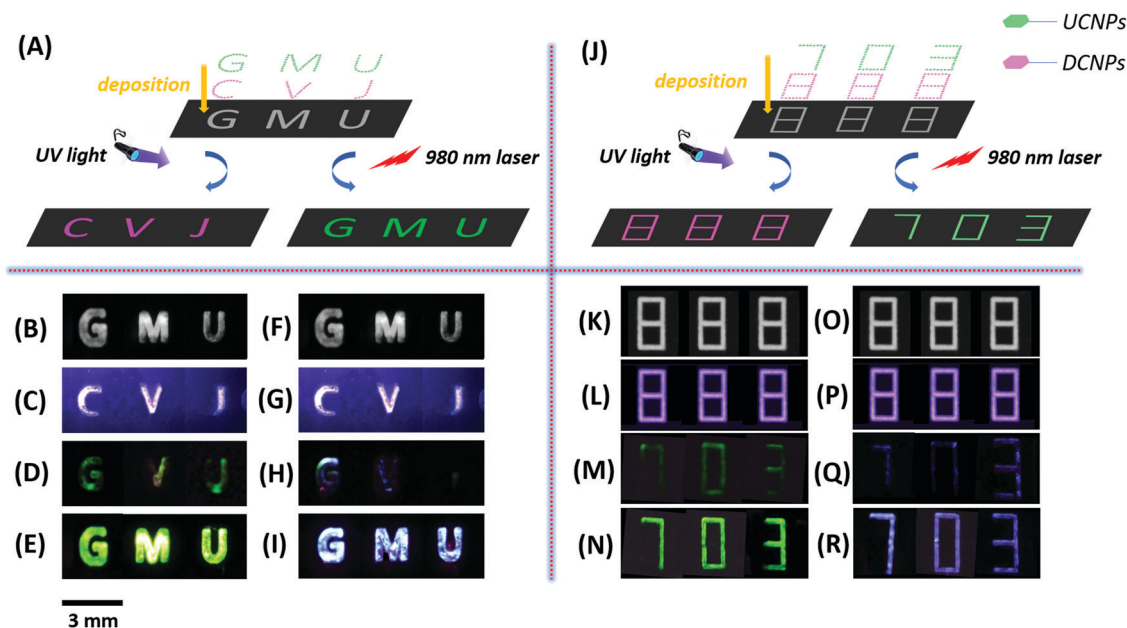
Fig. 6 (A) and (J) Schematic illustration of dual-modal manipulation of up- and down-conversion nanoparticles in anticounterfeiting applications. (B) and (F) Bright-field images of characters of "GMU" on polymethylmethacrylate (PMMA) plate. (C) and (G) Images of false information (CVJ) yielded by $NaGdF_4:Ce^{3+}@NaGdF_4:Eu^{3+}$ downconversion nanoparticles under excitation of ultraviolet light. (D) and (H) Images of true information (GMU) yielded by β-$NaYF_4:Yb^{3+}/Er^{3+}$ and β-$NaYF_4:Yb^{3+}/Tm^{3+}$ core UCNPs under excitation of 980 nm NIR laser, respectively. (E) and (I) Images of true information (GMU) yielded by β-$NaYF_4:Yb^{3+}/Er^{3+}@NaYF_4$ with 30 shell layers and β-$NaYF_4:Yb^{3+}/Tm^{3+}@NaYF_4$ with 30 shell layers UCNPs under excitation of 980 nm NIR laser, respectively. (K) and (O) Bright-field images of characters of "888" on PMMA plate. (L) and (P) False information (888) from $NaGdF_4:Ce^{3+}@NaGdF_4:Eu^{3+}$ downconversion nanoparticles under excitation of ultraviolet light. (M) and (Q) True information (703) from β-$NaYF_4:Yb^{3+}/Er^{3+}$ and β-$NaYF_4:Yb^{3+}/Tm^{3+}$ core UCNPs under excitation of 980 nm NIR laser, respectively. (N) and (R) True information (703) from β-$NaYF_4:Yb^{3+}/Er^{3+}@NaYF_4$ with 30 shell layers and β-$NaYF_4:Yb^{3+}/Tm^{3+}@NaYF_4$ with 30 shell layers UCNPs under excitation of 980 nm NIR laser, respectively. UCNPs and DCNPs represent upconversion and downconversion nanoparticles, respectively. (Power densities of UV lamp and 980 nm laser diode are 20 mW cm^{-2} and 6 W cm^{-2}, respectively.)

emission data in the experimentally measured photoluminescence spectra (Fig. 6D). The true pattern ("GMU") in the bright blue color is also obtained utilizing core–shell β-$NaYF_4:Yb^{3+}/Tm^{3+}@NaYF_4$ UCNPs with 30 layers in this encryption due to similarly enhanced upconverted blue emissions *via* SELF synthesis (Fig. 6I). To prove the universality and applicability of this dual-modal system, the same protocol is then extended to a PMMA plate with other engraved character marks such as "888" (Fig. 6J). The solution of multi-shelled UCNPs (β-$NaYF_4:Yb^{3+}/Er^{3+}@NaYF_4$ or β-$NaYF_4:Yb^{3+}/Tm^{3+}@NaYF_4$) is injected to label patterns "7", "0", and "3", corresponding to an area code of Virginia as the true information within the same character "8", while downconversion nanophosphor covers the whole pattern as the fake one (Fig. 6L, N, P and R). The consistency is further substantiated from the similar and satisfactory outcomes by simply alternating two excitation sources (254 nm and 980 nm) to distinguish the genuine information, which greatly enhances the anti-fake level.

3.5 Latent fingerprint imaging

The utilization of dual-mode systems in successful anticounterfeiting is mainly attributed to the strong upconverted luminescence brightness of the multi-shelled UCNPs *via* the SELF approach. Therefore, these multi-shelled UCNPs also have great potential in ultrasensitive fingerprint identification since clear and well-defined information can be readily visualized with the

naked eye when illuminated by brighter colors. In addition, the background interference can be effectively minimized under excitation of near-infrared laser. As one of the most useful types of direct biometric information, latent fingerprints (LFPs) have been widely applied in areas such as access control, personal identification, and medical diagnostics due to their invariance and uniqueness.[69–71] The accurate visualization of level 1 and level 2 details that describes the overall direction of the fingerprint ridge and specific ridge paths, respectively, is critical for identity recognition in forensic investigations.[72] In our work, multi-shelled UCNPs are used in the detection of a latent fingerprint deposited on smooth substrates such as transparent glass slides. Firstly, the as-prepared hydrophobic multi-shelled UCNPs (both Er^{3+} and Tm^{3+} doped) are transformed into hydrophilic particles dispersed in an aqueous phase by a facile ligand-exchange method using $NOBF_4$.[73] Secondly, the surface is modified with trisodium citrate to facilitate the imaging due to the electrostatic interaction, as well as to the constructive chemical reaction between the carboxyl groups (–COOH) on citrate-functionalized UCNPs and amine (–NH$_2$) groups of latent secretions. The complete removal of the original oleate ligands after treatment with $NOBF_4$ and subsequent modification with trisodium citrate are verified in FTIR spectra (Fig. S2, ESI†) by the appearance of the stretching bands of carbonyl groups (C=O) at 1397 cm^{-1} and 1588 cm^{-1}. The morphology and

This journal is © The Royal Society of Chemistry 2020

J. Mater. Chem. C, 2020, 8, 5692–5703 | 5699
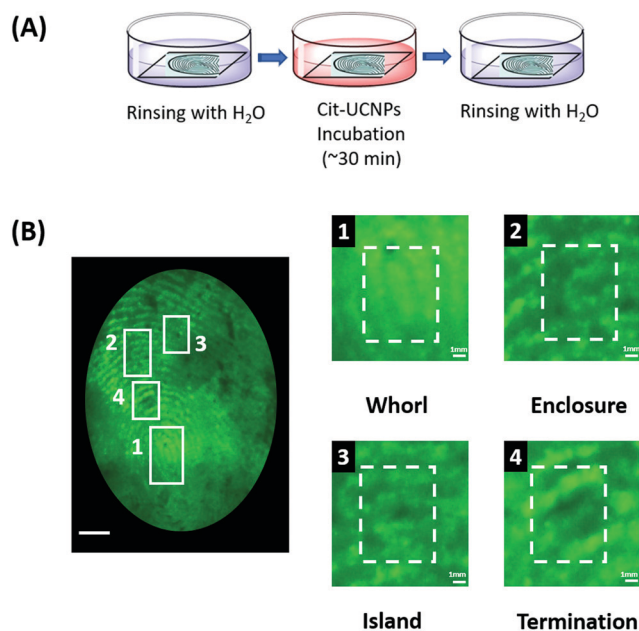
Fig. 7 (A) Schematic diagram of latent fingerprint incubation. (B) Image of illuminated latent fingerprint incubated with citrate functionalized 30-shell layered β-NaYF$_4$:Yb^{3+}/Er^{3+}@NaYF$_4$ UCNPs on glass slides under 980 nm excitation. The scale bar represents 2 mm. Magnified images of fingerprints with details including whorl (1), enclosure (2), island (3), and termination (4) under 980 nm excitation (power density: 3 W cm^{-2}).

emission intensities of hydrophilic UCNPs with 30 layers are maintained due to the formation of uniform shells *via* SELF approach (Fig. S3 and S4, ESI†). The incubation procedures are illustrated in Fig. 7A. Under irradiation of 980 nm laser, those specific ridge details considered as discriminative features, such as whorl (level 1), enclosure, island, and termination (level 2), are clearly revealed in the enlarged view of a fingerprint incubated with citrate functionalized core–shell β-NaYF$_4$:Yb^{3+}/Er^{3+}@NaYF$_4$ UCNPs with 30 layers (Fig. 7B). In distinct contrast, only a feeble and ambiguous image is observed for the fingerprint incubated with core UCNPs (Fig. S5, ESI†). At 980 nm, Tm^{3+}-doped core–shell UCNPs with 30 layers (β-NaYF$_4$:Yb^{3+}/Tm^{3+}@NaYF$_4$) show the similar results in latent fingerprint imaging with enhanced blue color in which pores and ridge patterns are recognized (Fig. S6 and S7, ESI†). Overall, our multi-shelled UCNPs (both Er^{3+} and Tm^{3+} doped) with substantially enhanced brightness *via* SELF protocol can serve as an ideal alternative for latent fingerprint detection by providing high contrast and sufficient details.

4. Conclusions

In summary, one-pot successive epitaxial layer-by-layer formation (SELF) strategy is introduced to synthesize a series of high-quality multi-shelled UCNPs with unimodal size distribution (coefficient of variation less than 5%). Maximum fold changes in emission intensities for Er^{3+}- and Tm^{3+}-doped multi-shelled UCNPs with 30 layers of shell reach as high as 300 and 200, respectively. A dual-mode luminescent system comprising of multi-shelled UCNPs and downconversion nanoparticles is developed and

utilized in anticounterfeiting to distinguish true information from fake patterns under irradiation of two excitation sources (980 nm and UV lamp). Latent fingerprint recognition with low background interference and distinguishable details in ridge patterns is also achieved taking advantage of the significantly enhanced upconverted photoluminescence. Therefore, we believe that SELF strategy will bring new opportunities in synthesizing and tailoring monodispersed UCNPs with improved brightness for more extensive applications in protection against forgery and information security.

Author contributions

Hao Jing designed the research. A. J. E. developed the one-pot successive epitaxial layer-by-layer formation (SELF) approach by synthesizing lanthanide-doped multi-shelled upconversion nanoparticles (UCNPs) and down-conversion nanocrystals, collected the photoluminescence and FTIR spectra, and took digital photographs of anti-counterfeiting applications including labelled character marks on PMMA plate as well as latent fingerprint imaging. M. I. assisted with the measurements and analysis of the results. A. F. M. performed the transmission electron microscopy (TEM) analyses on all nanoparticles. L. N. M. and G. K. P. analyzed the sizing and histogram of all nanoparticles. Hao Jing supervised the research. Hao Jing and A. J. E. co-wrote the paper. All authors discussed the results and commented on the manuscript.

Conflicts of interest

The authors declare no competing financial interest. This paper identifies certain commercial equipment, instruments, and materials to specify the experimental procedure. Such identification does not imply recommendation or endorsement by the National Institute of Standards and Technology, nor does it imply that the equipment, instruments, and materials identified are necessarily the best available for the purpose.

Acknowledgements

References

1 C. Fink, K. E. Maskus and Y. Qian, The Economic Effects of Counterfeiting and Piracy: A Review and Implications for Developing Countries, *World Bank Res. Obs.*, 2016, **31**, 1–28.

2 K. Degardin, Y. Roggo and P. Margot, Understanding and Fighting the Medicine Counterfeit Market, *J. Pharm. Biomed. Anal.*, 2014, **87**, 167–175.

5700 | *J. Mater. Chem. C*, 2020, **8**, 5692–5703

This journal is © The Royal Society of Chemistry 2020

3   B. Kumar and A. Baldi, The Challenge of Counterfeit Drugs: A Comprehensive Review on Prevalence, Detection and Preventive Measures, *Curr. Drug Saf.*, 2016, **11**, 112–120.

4   X. S. Hou, C. F. Ke, C. J. Bruns, P. R. McGonigal, R. B. Pettman and J. F. Stoddart, Tunable Solid-State Fluorescent Materials for Supramolecular Encryption, *Nat. Commun.*, 2015, **6**, 6884.

5   Y. H. Wen, T. L. Sheng, X. Q. Zhu, C. Zhuo, S. D. Su, H. R. Li, S. M. Hu, Q. L. Zhu and X. T. Wu, Introduction of Red-Green-Blue Fluorescent Dyes into a Metal–Organic Framework for Tunable White Light Emission, *Adv. Mater.*, 2017, **29**, 1700778.

6   F. Li, X. D. Wang, Z. G. Xia, C. F. Pan and Q. L. Liu, Photoluminescence Tuning in Stretchable Pdms Film Grafted Doped Core/Multishell Quantum Dots for Anticounterfeiting, *Adv. Funct. Mater.*, 2017, **27**, 1700051.

7   T. Han, Y. Yuan, X. Liang, Y. Zhang, C. X. Xiong and L. J. Dong, Colloidal Stable Quantum Dots Modified by Dual Functional Group Polymers for Inkjet Printing, *J. Mater. Chem. C*, 2017, **5**, 4629–4635.

8   L. T. Ling, L. Zhu, Q. Zhang, C. F. Wang and S. Chen, Interface-Spawned Nise Quantum Dots: Preparation, Photoluminescence Properties and Applications, *J. Mater. Chem. C*, 2015, **3**, 473–478.

9   L. M. Xu, J. W. Chen, J. Z. Song, J. H. Li, J. Xue, Y. H. Dong, B. Cai, Q. S. Shan, B. N. Han and H. B. Zeng, Double-Protected All-Inorganic Perovskite Nanocrystals by Crystalline Matrix and Silica for Triple-Modal Anti-Counterfeiting Codes, *ACS Appl. Mater. Interfaces*, 2017, **9**, 26556–26564.

10 C. Y. Zhang, B. Wang, W. B. Li, S. Q. Huang, L. Kong, Z. C. Li and L. Li, Conversion of Invisible Metal–Organic Frameworks to Luminescent Perovskite Nanocrystals for Confidential Information Encryption and Decryption, *Nat. Commun.*, 2017, **8**, 1138.

11 H. C. Liu, M. K. G. Jayakumar, K. Huang, Z. Wang, X. Zheng, H. Agren and Y. Zhang, Phase Angle Encoded Upconversion Luminescent Nanocrystals for Multiplexing Applications, *Nanoscale*, 2017, **9**, 1676–1686.

12 B. Chen and F. Wang, Combating Concentration Quenching in Upconversion Nanoparticles, *Acc. Chem. Res.*, 2020, **53**, 358–367.

13 D. R. Gamelin and H. U. Gudel, Upconversion Processes in Transition Metal and Rare Earth Metal Systems, *Top. Curr. Chem.*, 2001, **214**, 1–56.

14 X. Qin, X. W. Liu, W. Huang, M. Bettinelli and X. G. Liu, Lanthanide-Activated Phosphors Based on 4f–5d Optical Transitions: Theoretical and Experimental Aspects, *Chem. Rev.*, 2017, **117**, 4488–4527.

15 B. Zhou, B. Y. Shi, D. Y. Jin and X. G. Liu, Controlling Upconversion Nanocrystals for Emerging Applications, *Nat. Nanotechnol.*, 2015, **10**, 924–936.

16 X. Qin, J. H. Xu, Y. M. Wu and X. G. Liu, Energy-Transfer Editing in Lanthanide-Activated Upconversion Nanocrystals: A Toolbox for Emerging Applications, *ACS Cent. Sci.*, 2019, **5**, 29–42.

17 J. Zhou, Q. Liu, W. Feng, Y. Sun and F. Y. Li, Upconversion Luminescent Materials: Advances and Applications, *Chem. Rev.*, 2015, **115**, 395–465.

18 G. Y. Chen, H. L. Qiu, P. N. Prasad and X. Y. Chen, Upconversion Nanoparticles: Design, Nanochemistry, and Applications in Theranostics, *Chem. Rev.*, 2014, **114**, 5161–5214.

19 H. Dong, S. R. Du, X. Y. Zheng, G. M. Lyu, L. D. Sun, L. D. Li, P. Z. Zhang, C. Zhang and C. H. Yan, Lanthanide Nanoparticles: From Design toward Bioimaging and Therapy, *Chem. Rev.*, 2015, **115**, 10725–10815.

20 N. Bloembergen, Solid State Infrared Quantum Counters, *Phys. Rev. Lett.*, 1959, **2**, 84–85.

21 V. V. Ovsyakin and P. P. Feofilov, Cooperative Sensitization of Luminescence in Crystals Activated with Rare Earth Ions, *JETP Lett.*, 1966, **4**, 317–318.

22 F. Auzel, Upconversion and Anti-Stokes Processes with F and D Ions in Solids, *Chem. Rev.*, 2004, **104**, 139–173.

23 D. L. Zhou, D. Y. Li, X. Y. Zhou, W. Xu, X. Chen, D. L. Liu, Y. S. Zhu and H. W. Song, Semiconductor Plasmon Induced up-Conversion Enhancement in $mCu_{2-x}S@SiO_2@Y_2O_3$:Yb^{3+}/Er^{3+} Core–Shell Nanocomposites, *ACS Appl. Mater. Interfaces*, 2017, **9**, 35226–35233.

24 Y. D. Han, H. Y. Li, Y. B. Wang, Y. Pan, L. Huang, F. Song and W. Huang, Upconversion Modulation through Pulsed Laser Excitation for Anticounterfeiting, *Sci. Rep.*, 2017, **7**, 1320.

25 L. Lei, D. Q. Chen, C. Li, F. Huang, J. J. Zhang and S. Q. Xu, Inverse Thermal Quenching Effect in Lanthanide-Doped Upconversion Nanocrystals for Anti-Counterfeiting, *J. Mater. Chem. C*, 2018, **6**, 5427–5433.

26 C. D. S. Brites, X. J. Xie, M. L. Debasu, X. Qin, R. F. Chen, W. Huang, J. Rocha, X. G. Liu and L. D. Carlos, Instantaneous Ballistic Velocity of Suspended Brownian Nanocrystals Measured by Upconversion Nanothermometry, *Nat. Nanotechnol.*, 2016, **11**, 851–856.

27 Y. Q. Lu, J. B. Zhao, R. Zhang, Y. J. Liu, D. M. Liu, E. M. Goldys, X. S. Yang, P. Xi, A. Sunna, J. Lu, Y. Shi, R. C. Leif, Y. J. Huo, J. Shen, J. A. Piper, J. P. Robinson and D. Y. Jin, Tunable Lifetime Multiplexing Using Luminescent Nanocrystals, *Nat. Photonics*, 2014, **8**, 33–37.

28 H. Dong, L. D. Sun, W. Feng, Y. Y. Gu, F. Y. Li and C. H. Yan, Versatile Spectral and Lifetime Multiplexing Nanoplatform with Excitation Orthogonalized Upconversion Luminescence, *ACS Nano*, 2017, **11**, 3289–3297.

29 X. W. Liu, Y. Wang, X. Y. Li, Z. G. Yi, R. R. Deng, L. L. Liang, X. J. Xie, D. T. B. Loong, S. Y. Song, D. Y. Fan, A. H. All, H. J. Zhang, L. Huang and X. G. Liu, Binary Temporal Upconversion Codes of Mn^{2+}-Activated Nanoparticles for Multilevel Anti-Counterfeiting, *Nat. Commun.*, 2017, **8**, 899.

30 J. Lee, P. W. Bisso, R. L. Srinivas, J. J. Kim, A. J. Swiston and P. S. Doyle, Universal Process-Inert Encoding Architecture for Polymer Microparticles, *Nat. Mater.*, 2014, **13**, 524–529.

31 Y. H. Zhang, L. X. Zhang, R. R. Deng, J. Tian, Y. Zong, D. Y. Jin and X. G. Liu, Multicolor Barcoding in a Single Upconversion Crystal, *J. Am. Chem. Soc.*, 2014, **136**, 4893–4896.

32 J. M. Meruga, A. Baride, W. Cross, J. J. Kellar and P. S. May, Red-Green-Blue Printing Using Luminescence-Upconversion Inks, *J. Mater. Chem. C*, 2014, **2**, 2221–2227.

33 F. Kaholi, N. Ghazyani, M. Riahi, H. Zare-Behtash, M. H. M. Ara and E. Heydari, Upconverting Nanoengineered

This journal is © The Royal Society of Chemistry 2020

J. Mater. Chem. C, 2020, **8**, 5692–5703 | **5701**

Surfaces: Maskless Photolithography for Security Applications, *ACS Appl. Nano Mater.*, 2019, **2**, 3590–3596.

34 E. D. Martinez, R. R. Urbane and C. Rettori, Thermoplasmonic Maskless Lithography on Upconverting Nanocomposites Assisted by Gold Nanostars, *ACS Appl. Nano Mater.*, 2019, **2**, 6889–6897.

35 Y. M. Wu, M. J. Y. Ang, M. Z. Sun, B. L. Huang and X. G. Liu, Expanding the Toolbox for Lanthanide-Doped Upconversion Nanocrystals, *J. Phys. D: Appl. Phys.*, 2019, **52**, 383002.

36 S. Fischer, N. D. Bronstein, J. K. Swabeck, E. M. Chan and A. P. Alivisatos, Precise Tuning of Surface Quenching for Luminescence Enhancement in Core–Shell Lanthanide-Doped Nanocrystals, *Nano Lett.*, 2016, **16**, 7241–7247.

37 N. J. J. Johnson, S. He, S. Diao, E. M. Chan, H. J. Dai and A. Almutairi, Direct Evidence for Coupled Surface and Concentration Quenching Dynamics in Lanthanide-Doped Nanocrystals, *J. Am. Chem. Soc.*, 2017, **139**, 3275–3282.

38 M. D. Wisser, S. Fischer, C. Siefe, A. P. Alivisatos, A. Salleo and J. A. Dionne, Improving Quantum Yield of Upconverting Nanoparticles in Aqueous Media Via Emission Sensitization, *Nano Lett.*, 2018, **18**, 2689–2695.

39 F. Wang, J. A. Wang and X. G. Liu, Direct Evidence of a Surface Quenching Effect on Size-Dependent Luminescence of Upconversion Nanoparticles, *Angew. Chem., Int. Ed.*, 2010, **49**, 7456–7460.

40 F. Chen, W. B. Bu, S. J. Zhang, X. H. Liu, J. N. Liu, H. Y. Xing, Q. F. Xiao, L. P. Zhou, W. J. Peng, L. Z. Wang and J. L. Shi, Positive and Negative Lattice Shielding Effects Co-Existing in Gd(III) Ion Doped Bifunctional Upconversion Nanoprobes, *Adv. Funct. Mater.*, 2011, **21**, 4285–4294.

41 H. X. Mai, Y. W. Zhang, L. D. Sun and C. H. Yan, Highly Efficient Multicolor up-Conversion Emissions and Their Mechanisms of Monodisperse NaYF₄:Yb,Er Core and Core/Shell-Structured Nanocrystals, *J. Phys. Chem. C*, 2007, **111**, 13721–13729.

42 Y. S. Liu, D. T. Tu, H. M. Zhu, R. F. Li, W. Q. Luo and X. Y. Chen, A Strategy to Achieve Efficient Dual-Mode Luminescence of Eu^{3+} in Lanthanides Doped Multifunctional $NaGdF_4$ Nanocrystals, *Adv. Mater.*, 2010, **22**, 3266–3271.

43 F. Zhang, R. C. Che, X. M. Li, C. Yao, J. P. Yang, D. K. Shen, P. Hu, W. Li and D. Y. Zhao, Direct Imaging the Upconversion Nanocrystal Core/Shell Structure at the Subnanometer Level: Shell Thickness Dependence in Upconverting Optical Properties, *Nano Lett.*, 2012, **12**, 2852–2858.

44 G. Tessitore, G. A. Mandl, M. G. Brik, W. Park and J. A. Capobianco, Recent Insights into Upconverting Nanoparticles: Spectroscopy, Modeling, and Routes to Improved Luminescence, *Nanoscale*, 2019, **11**, 12015–12029.

45 B. Chen and F. Wang, Emerging Frontiers of Upconversion Nanoparticles, *Trends Chem.*, 2020, **2**, DOI: 10.1016/j.trechm.2020.01.008.

46 K. A. Abel, J. C. Boyer and F. van Veggel, Hard Proof of the $NaYF_4/NaGdF_4$ Nanocrystal Core/Shell Structure, *J. Am. Chem. Soc.*, 2009, **131**, 14644–14645.

47 K. A. Abel, J. C. Boyer, C. M. Andrei and F. van Veggel, Analysis of the Shell Thickness Distribution on $NaYF_4/NaGdF_4$

Core/Shell Nanocrystals by EELS and EDS, *J. Phys. Chem. Lett.*, 2011, **2**, 185–189.

48 C. H. Dong, A. Korinek, B. Blasiak, B. Tomanek and F. van Veggel, Cation Exchange: A Facile Method to Make $NaYF_4$: Yb,Tm-$NaGdF_4$ Core–Shell Nanoparticles with a Thin, Tunable, and Uniform Shell, *Chem. Mater.*, 2012, **24**, 1297–1305.

49 F. Wang, R. R. Deng, J. Wang, Q. X. Wang, Y. Han, H. M. Zhu, X. Y. Chen and X. G. Liu, Tuning Upconversion through Energy Migration in Core–Shell Nanoparticles, *Nat. Mater.*, 2011, **10**, 968–973.

50 X. M. Li, D. K. Shen, J. P. Yang, C. Yao, R. C. Che, F. Zhang and D. Y. Zhao, Successive Layer-by-Layer Strategy for Multi-Shell Epitaxial Growth: Shell Thickness and Doping Position Dependence in Upconverting Optical Properties, *Chem. Mater.*, 2013, **25**, 106–112.

51 S. Y. Han, X. Qin, Z. F. An, Y. H. Zhu, L. L. Liang, Y. Han, W. Huang and X. G. Liu, Multicolour Synthesis in Lanthanide-Doped Nanocrystals through Cation Exchange in Water, *Nat. Commun.*, 2016, **7**, 13059.

52 T. Y. Sun, B. Z. Xu, B. Chen, X. Chen, M. Y. Li, P. Shi and F. Wang, Anti-Counterfeiting Patterns Encrypted with Multi-Mode Luminescent Nanotaggants, *Nanoscale*, 2017, **9**, 2701–2705.

53 L. Zhou, Y. Fan, R. Wang, X. M. Li, L. L. Fan and F. Zhang, High-Capacity Upconversion Wavelength and Lifetime Binary Encoding for Multiplexed Biodetection, *Angew. Chem., Int. Ed.*, 2018, **57**, 12824–12829.

54 L. Liu, S. F. Wang, B. Z. Zhao, P. Pei, Y. Fan, X. M. Li and F. Zhang, Er^{3+} Sensitized 1530 nm to 1180 nm Second near-Infrared Window Upconversion Nanocrystals for *in vivo* Biosensing, *Angew. Chem., Int. Ed.*, 2018, **57**, 7518–7522.

55 H. X. Zhang, Y. Fan, P. Pei, C. X. Sun, L. F. Lu and F. Zhang, Tm^{3+}-Sensitized NIR-II Fluorescent Nanocrystals for *in Vivo* Information Storage and Decoding, *Angew. Chem., Int. Ed.*, 2019, **58**, 10153–10157.

56 Y. Fan, P. Y. Wang, Y. Q. Lu, R. Wang, L. Zhou, X. L. Zheng, X. M. Li, J. A. Piper and F. Zhang, Lifetime-Engineered NIR-II Nanoparticles Unlock Multiplexed *in Vivo* Imaging, *Nat. Nanotechnol.*, 2018, **13**, 941–946.

57 M. Y. Zhao, B. H. Li, P. Y. Wang, L. F. Lu, Z. C. Zhang, L. Liu, S. F. Wang, D. D. Li, R. Wang and F. Zhang, Supramolecularly Engineered NIR-II and Upconversion Nanoparticles *in Vivo* Assembly and Disassembly to Improve Bioimaging, *Adv. Mater.*, 2018, 30.

58 M. Y. Ding, D. Q. Chen, Z. Y. Wan, Y. Zhou, J. S. Zhong, J. H. Xi and Z. G. Ji, Achieving Efficient Tb^{3+} Dual-Mode Luminescence Via Gd-Sublattice-Mediated Energy Migration in a $NaGdF_4$ Core–Shell Nanoarchitecture, *J. Mater. Chem. C*, 2015, **3**, 5372–5376.

59 P. Li, Q. Peng and Y. D. Li, Dual-Mode Luminescent Colloidal Spheres from Monodisperse Rare-Earth Fluoride Nanocrystals, *Adv. Mater.*, 2009, **21**, 1945–1948.

60 J. Xu, B. B. Zhang, L. Jia, Y. P. Fan, R. J. Chen, T. H. Zhu and B. Z. Liu, Dual-Mode, Color-Tunable, Lanthanide-Doped Core–Shell Nanoarchitectures for Anti-Counterfeiting Inks and Latent Fingerprint Recognition, *ACS Appl. Mater. Interfaces*, 2019, **11**, 35294–35304.

5702 | *J. Mater. Chem. C*, 2020, **8**, 5692–5703

This journal is © The Royal Society of Chemistry 2020

61 Y. D. Han, C. Gao, Y. B. Wang, D. D. Ju, A. H. Zhou, F. Song, L. Huang and W. Huang, Spatially Confined Luminescence Process in Tip-Modified Heterogeneous-Structured Micro-rods for High-Level Anti-Counterfeiting, *Phys. Chem. Chem. Phys.*, 2018, **20**, 9516–9522.

62 S. W. Xie, G. Gong, Y. Song, H. H. Tan, C. F. Zhang, N. Li, Y. X. Zhang, L. J. Xu, J. X. Xu and J. Zheng, Design of Novel Lanthanide-Doped Core–Shell Nanocrystals with Dual up-Conversion and Down-Conversion Luminescence for Anti-Counterfeiting Printing, *Dalton Trans.*, 2019, **48**, 6971–6983.

63 J.-C. G. E. Bünzli and V. Svetlana, in Basics of Lanthanide Photophysics, *Lanthanide Luminescence*, ed. P. H. H. Härmä, Springer, 2010, vol. 7, pp. 1–45.

64 L. D. Sun, H. Dong, P. Z. Zhang and C. H. Yan, Upconversion of Rare Earth Nanomaterials, *Annu. Rev. Phys. Chem.*, 2015, **66**, 619–642.

65 M. Li, X. Y. Liu, L. Liu, B. Ma, B. X. Li, X. D. Zhao, W. M. Tong and X. F. Wang, Beta-NaYF$_4$:Yb,Tm: Upconversion Properties by Controlling the Transition Probabilities at the Same Energy Level, *Inorg. Chem. Front.*, 2016, **3**, 1082–1090.

66 B. Ma, X. Y. Liu, L. Liu, Y. J. Meng, B. X. Li, X. D. Zhao, P. X. Pu and X. F. Wang, Special Tm^{3+} Transition and White Upconversion Luminescence in the Yb^{3+}/Tm^{3+} Co-Doped KMnF$_3$, *RSC Adv.*, 2014, **4**, 63100–63104.

67 T. A. A. Assumpcao, D. M. da Silva, L. R. P. Kassab and C. B. de Araujo, Frequency Upconversion Luminescence from Yb^{3+}–Tm^{3+} Codoped PbO–GeO$_2$ Glasses Containing Silver Nanoparticles, *J. Appl. Phys.*, 2009, **106**.

68 R. T. Wegh, H. Donker, K. D. Oskam and A. Meijerink, Visible Quantum Cutting in LiGdF$_4$:Eu^{3+} through Down-conversion, *Science*, 1999, **283**, 663–666.

69 J. Wang, T. Wei, X. Y. Li, B. H. Zhang, J. X. Wang, C. Huang and Q. Yuan, Near-Infrared-Light-Mediated Imaging of Latent Fingerprints Based on Molecular Recognition, *Angew. Chem., Int. Ed.*, 2014, **53**, 1616–1620.

70 P. Hazarika and D. A. Russell, Advances in Fingerprint Analysis, *Angew. Chem., Int. Ed.*, 2012, **51**, 3524–3531.

71 J. Hai, T. R. Li, J. X. Su, W. S. Liu, Y. M. Ju, B. D. Wang and Y. L. Hou, Reversible Response of Luminescent Terbium(III)-Nanocellulose Hydrogels to Anions for Latent Fingerprint Detection and Encryption, *Angew. Chem., Int. Ed.*, 2018, **57**, 6786–6790.

72 Y. Q. Wang, J. Wang, Q. Q. Ma, Z. H. Li and Q. Yuan, Recent Progress in Background-Free Latent Fingerprint Imaging, *Nano Res.*, 2018, **11**, 5499–5518.

73 A. G. Dong, X. C. Ye, J. Chen, Y. J. Kang, T. Gordon, J. M. Kikkawa and C. B. Murray, A Generalized Ligand-Exchange Strategy Enabling Sequential Surface Functionalization of Colloidal Nanocrystals, *J. Am. Chem. Soc.*, 2011, **133**, 998–1006.

This journal is © The Royal Society of Chemistry 2020

J. Mater. Chem. C, 2020, **8**, 5692–5703 | **5703**